PCCP

Cite this: *Phys. Chem. Chem. Phys.*, 2012, **14**, 3996–4010

www.rsc.org/pccp

PAPER

Desorption of alkali atoms from ^{4}He nanodroplets

Alberto Hernando,†[a] Manuel Barranco,[a] Martí Pi,[a] Evgeniy Loginov,[b] Marina Langlet[b] and Marcel Drabbels*[b]

Received 9th November 2011, Accepted 12th January 2012
DOI: 10.1039/c2cp23526a

The dynamics following the photoexcitation of Na and Li atoms located on the surface of helium nanodroplets has been investigated in a joint experimental and theoretical study. Photoelectron spectroscopy has revealed that excitation of the alkali atoms *via* the $(n + 1)$s $\leftarrow$ ns transition leads to the desorption of these atoms. The mean kinetic energy of the desorbed atoms, as determined by ion imaging, shows a linear dependence on excitation frequency. These experimental findings are analyzed within a three-dimensional, time-dependent density functional approach for the helium droplet combined with a Bohmian dynamics description of the desorbing atom. This hybrid method reproduces well the key experimental observables. The dependence of the observables on the impurity mass is discussed by comparing the results obtained for the ^{6}Li and ^{7}Li isotopes. The calculations show that the desorption of the excited alkali atom is accompanied by the creation of highly non-linear density waves in the helium droplet that propagate at supersonic velocities.

I. Introduction

During the last decade, many properties of helium droplets have been disclosed, especially in relation to their use as a gentle matrix for spectroscopic experiments. In particular, the dynamical aspects associated with the vibrational and rotational degrees of freedom of embedded chromophores, as probed by infrared spectroscopy, are nowadays well established. We refer the interested reader to a series of review papers devoted to this subject.[1–8] At variance, the effect of the strong perturbations induced by electronic excitation or ionization of impurities in helium droplets is much less understood. For example, there is still no consistent model that can fully account for the lineshapes and splittings observed in the electronic spectra of aromatic molecules.[9] Even less is known about the ensuing dynamics, like the rearrangement of the helium or the evolution of photoelectrons.[10] These aspects are however expected to be relevant for the study of chemical reactions in this soft ultracold environment, since chemical reactions involve essentially the rearrangement of the electronic structure of reactants. In this respect, understanding the dynamical evolution of an electronically excited impurity in helium droplets might be considered a first step towards a better understanding of chemical reactions in this unique quantum environment.

The aim of the present work is to gain insight into the dynamics initiated by the excitation of alkali atoms residing on the surface of helium droplets. The np $\leftarrow$ ns transitions of alkali-doped helium nanodroplets have been the subject of a series of experimental and theoretical studies, see *e.g.* ref. 11–15 and references therein. Only recently, studies involving transitions to higher excited states have been reported.[16–18] These studies reveal that excitation of the alkali atoms in almost all cases leads to the desorption of the excited atoms from the surface of the helium droplet on a picosecond timescale.[19,20] In the present work we investigate, both experimentally and theoretically, the desorption process of Na and Li atoms following excitation to the 4s and 3s state, respectively. The use of two different atomic systems allows us to identify general processes, while the use of lithium having two light isotopes, ^{6}Li and ^{7}Li, allows us to quantify the mass effect on these processes. In the experiments we have used ion and electron imaging techniques to determine the state distributions of the desorbed atoms and the velocity distributions of these atoms as a function of excitation frequency. The functional correlation between excitation energy and final kinetic energy of the impurities has also been determined from first principles using Fermi's Golden Rule. The dynamics of the desorption process has been modeled using a newly developed theoretical hybrid approach based on time-dependent DFT for the helium density and quantum trajectories for the impurity wave function.

The hydrodynamic formulation of quantum mechanics—first developed by Bohm[21]—has drawn the attention of theoretical quantum chemists and physicists because it constitutes an alternative representation to the time-dependent Schrödinger

[a] *Departament ECM, Facultat de Física, and IN^{2}UB, Universitat de Barcelona, Diagonal 647, 08028 Barcelona, Spain*
[b] *Laboratoire de Chimie Physique Moléculaire, Swiss Federal Institute of Technology Lausanne (EPFL), CH-1015 Lausanne, Switzerland. E-mail: marcel.drabbels@epfl.ch*
† Present address: Laboratoire Collisions, Agrégats, Réactivité, IRSAMC, Université Paul Sabatier 118 route de Narbonne 31062 - Toulouse CEDEX 09, France.

equation that allows us to overcome some of the computational problems inherent to the conventional quantum mechanical approach.[22] The Bohmian formulation bears a large flexibility, and a variety of quantum trajectory methods are found in the literature, each of them adapted to the nature of the dynamical problem under investigation.[22–26] We will show how the Bohmian method also lends itself to the study of the complex dynamical processes addressed in the present work.

This paper is organized as follows. In Section II we describe the experimental setup. The quantum-trajectory model developed here to analyze the experimental results is presented in Section III. In Section IV the experimental results are presented and compared with the outcome of the calculations. Further remarks on the results are made in Section V, and we conclude with a summary, Section VI. Finally, a brief theoretical discussion on the angular dependence of the velocity distributions is presented in Appendix A, and the expressions used to simulate the experimental observables are collected in Appendix B.

II. Experimental

The experimental setup has been described in detail before.[27,28] In brief, helium droplets consisting on average of several thousands of atoms are formed by expanding high-purity helium gas at a pressure of 30 bar into vacuum through a 5 μm orifice cooled to cryogenic temperatures. The size distribution of these droplets can be systematically varied by changing the source temperature.[29] The helium droplets pick up alkali atoms as they traverse an oven in which either sodium or lithium metal is evaporated. The temperature of the oven is adjusted to ensure that the droplets on average pick up less than one alkali atom. *Via* a differential pumping stage the doped droplets enter a velocity map imaging spectrometer. At the center of this setup, the alkali-doped droplets are excited by crossing the droplet beam perpendicularly with the frequency-doubled output of a Nd:YAG pumped dye laser (PrecisionScan SL, Sirah Laser- und Plasmatechnik GmbH). The laser system is operated at a repetition frequency of 20 Hz and provides radiation with a linewidth of less than 0.1 cm^{-1}, an energy of 5 mJ per pulse and a pulse duration of 11 ± 1 ns. The laser beam is slightly focused to yield an estimated spot size of 0.37 mm^2 at the excitation region. Following excitation, the alkali atoms are ionized by the absorption of an additional photon from the same laser pulse. The ions, or alternatively the photoelectrons, are accelerated by the applied electric fields and projected onto a position sensitive detector consisting of a pair of microchannel plates and a phosphor screen. The light emitted by the phosphor screen is imaged onto a high-resolution CCD camera (A202k, Basler) that is read out every laser shot. The individual images are analyzed online and the centroids of the impacts are determined. The kinetic energy distributions are determined by performing an inverse Abel transform on the image constructed from the accumulated centroids. Spectra are recorded using this setup by monitoring the number of ion impacts on the detector as a function of laser frequency. Both the ion images and the spectra can be recorded at a specific mass by gating the front of the detector at the arrival time of the ions of interest.

III. Theoretical approach

The theoretical model is described here in detail for the 4s ← 3s excitation of Na impurities on ^{4}He droplets, but the formalism applies equally well to the corresponding 3s ← 2s transition in lithium. We would like to point out that, while the $(n + 1)$s ← ns transitions are dipole forbidden in the gas phase, they are allowed when the atoms reside on the surface of helium droplets due to the reduced symmetry of the system.[17]

Our starting point is the Fermi Golden Rule (GR) for optical transitions derived from perturbation theory.[30] It yields the transition probability per unit time $w_{i\to f}$ from an initial state $|i\rangle$ to a final state $|f\rangle$ due to the interaction with a perturbative electromagnetic field $H_I(t) = e^{-i\omega t}V_I$ in a time interval T:

$$w_{i\to f}(\omega) = \frac{1}{\hbar^2 T}\left|\int_T \mathrm{d}t e^{-i\omega t}\langle f|e^{i\mathscr{H}t/\hbar}V_I e^{-i\mathscr{H}t/\hbar}|i\rangle\right|^2, \qquad (1)$$

where $\mathscr{H}$ is the unperturbed hamiltonian that describes the system. For our purpose here, the initial state is the ground state (gs) of the complex consisting of a superfluid ^{4}He droplet and a Na atom at zero temperature. We label it as $|i\rangle = |\Psi_{\mathrm{He}}^{\mathrm{gs}},\psi_{\mathrm{Na}}^{\mathrm{gs}},\varphi_{\mathrm{e}}^{3\mathrm{s}}\rangle$, where Ψ_{He} is the nuclear many-body wave function of the helium cluster, ψ_{Na} the nuclear wave function of the sodium atom, and φ_{e} the electronic wave function of the complex. For convenience, we make explicit that the Na valence electron is in the nominal 3s state, as it is this electron that interacts with the electromagnetic field. We are interested in those final states $|f\rangle$ that are accessible by the optical transition to the nominal 4s state and we hence label them as $|f\rangle = |\Psi_{\mathrm{He}}^{f},\psi_{\mathrm{Na}}^{f},\varphi_{\mathrm{e}}^{4\mathrm{s}}\rangle$.

To evaluate the integrand of the GR we make the following approximations:

(i) The Born–Oppenheimer (BO) approximation[30] is used to factorize the electronic and nuclear wavefunctions.

(ii) Density functional theory (DFT)[4,31] is used to describe the droplet-impurity complex, factorizing the Na and He nuclear wavefunctions, both evolving according to self-consistent mean-field hamiltonians.

(iii) The Franck–Condon (FC) principle[30] is invoked, so that it can be assumed that the atomic nuclei do not change their positions or momenta during the electronic transition.

A. The electronic contribution

The BO approximation allows one to factorize the electronic contribution in the GR expression as $|\langle\varphi_{\mathrm{e}}^{4\mathrm{s}}|V_I|\varphi_{\mathrm{e}}^{3\mathrm{s}}\rangle|^2$, and to use effective pair-potentials for the nuclear hamiltonians. Due to the dipolar nature of the transition, the angular dependence of $|\langle\varphi_{\mathrm{e}}^{4\mathrm{s}}|V_I|\varphi_{\mathrm{e}}^{3\mathrm{s}}\rangle|^2$ can be written as $P(\theta) = \frac{1}{4\pi}[1 + \beta P_2(\cos\theta)]$,[32,33] where $P_2(x)$ is the second Legendre polynomial, θ is the angle between the direction of the polarization vector of the laser light and the final velocity of the adatom, and β is the so-called anisotropy parameter.

Since the projection of the orbital angular momentum onto the symmetry axis of the system—defined by the sodium atom and the center-of-mass of the helium droplet—does not change during the electronic transition, the value of β can be

inferred by considering the symmetry of the valence electron wavefunctions, φ_e^{3s} and φ_e^{4s}. Under the assumption that both these nominally spherical wavefunctions exhibit a dipolar deformation and that this deformation is larger for the final wavefunction φ_e^{4s} as a result of the stronger interaction with the helium cluster,[17] one finds that the value of the anisotropy parameter is limited to $1.5 < \beta < 2$, see Appendix A.

B. The nuclear contribution within DFT

For the nuclear contribution, we start from the DFT description of the system in its ground state as described *e.g.* in ref. 4 and 31. We want to recall here that this is a zero temperature phenomenological description of superfluid liquid ^{4}He that reproduces its thermodynamic properties and elementary excitation spectrum. The BO factorization of the electronic wavefunction allows one to represent the interaction between the helium moiety and the impurity by an effective He–Na interaction which is based on the $V_X^{3s}(r_{He-Na})$ pair-potential, r_{He-Na} being the interatomic distance.[34] From the minimization of the energy density functional $E[\Psi_{He},\psi_{Na}]$, we obtain the effective hamiltonians corresponding to both the helium particle density $\rho_{He}(\mathbf{r}) = |\Psi_{He}(\mathbf{r})|^2$, and the Na wavefunction $\psi_{Na}(\mathbf{r})$:

$$\begin{aligned} H_{He}^{3s}\Psi_{He}(\mathbf{r}) &\equiv \left\{-\frac{\hbar^2\nabla^2}{2m_{He}} + U[\rho_{He}] + V_{He}^{3s}(\mathbf{r})\right\}\Psi_{He}(\mathbf{r}) \\ &= \mu\Psi_{He}(\mathbf{r}) \\ H_{Na}^{3s}\psi_{Na}(\mathbf{r}) &\equiv \left\{-\frac{\hbar^2\nabla^2}{2m_{Na}} + V_{Na}^{3s}(\mathbf{r})\right\}\psi_{Na}(\mathbf{r}) \\ &= \varepsilon_{gs}\psi_{Na}(\mathbf{r}). \end{aligned} \quad (2)$$

Here, $U[\rho_{He}]$ is the helium DFT self-consistent potential, μ the helium chemical potential and ε_{gs} the ground state eigenenergy of the sodium atom in the mean field created by the helium droplet. The mean field interaction potentials are obtained by convolution

$$\begin{aligned} V_{He}^{3s}(\mathbf{r}) &= \int d\mathbf{r}'|\psi_{Na}(\mathbf{r}')|^2 V_X^{3s}(|\mathbf{r}' - \mathbf{r}|) \\ V_{Na}^{3s}(\mathbf{r}) &= \int d\mathbf{r}'|\Psi_{He}(\mathbf{r}')|^2 V_X^{3s}(|\mathbf{r}' - \mathbf{r}|). \end{aligned} \quad (3)$$

These density-dependent, mean field hamiltonians are employed to find the ground state of the droplet-impurity complex—Ψ_{He}^{gs} and ψ_{Na}^{gs}—used in the evaluation of the GR. Within the FC approximation the helium density is frozen, which allows us to identify Ψ_{He}^{f} with Ψ_{He}^{gs} and to write the total transition probability as

$$w_{i\to f}(\omega) \propto [1 + \beta P_2(\cos\theta)] \times I(\omega, f) \quad (4)$$

with

$$I(\omega,f) = \frac{1}{T}\left|\int_T dt e^{-i(\omega+\omega_{gs})t}\langle\psi_{Na}^{f}|e^{iH_{Na}^{4s}t/\hbar}|\psi_{Na}^{gs}\rangle\right|^2. \quad (5)$$

Here, $\hbar\omega_{gs} = \varepsilon_{gs}$, and H_{Na}^{4s} is the effective hamiltonian for the excited impurity, calculated by evaluating eqn (3) using the ground state helium density and the the excited state pair-potential $V^{4s}(r_{He-Na})$ of ref. 35. Introducing the identity $\sum_n|n\rangle\langle n| = 1$, where $\{|n\rangle\}$ is a complete set of H_{Na}^{4s} eigenstates with eigenenergies $\hbar\omega_{n0}$, we obtain

$$I(\omega,f) = \sum_n |\langle\psi_{Na}^{f}|n\rangle|^2 \times |\langle n|\psi_{Na}^{gs}\rangle|^2\delta[\omega - (\omega_n - \omega_{gs})]. \quad (6)$$

It is worth noting that summing eqn (6) over the final states f one obtains the Franck–Condon factors for the Na absorption spectrum[36–38]

$$I(\omega) = \sum_f I(\omega,f) = \sum_n |\langle n|\psi_{Na}^{gs}\rangle|^2\delta[\omega - (\omega_n - \omega_{gs})]. \quad (7)$$

As previously indicated, the final states ψ_{Na}^{f} are those accessible by the optical transition to the nominal 4s state. By using the same $|n\rangle$ basis for the final states we recover from eqn (6) the Franck–Condon factors. However, in the ion imaging experiments discussed below what are probed are adatoms after their desorption from the helium cluster, which are characterized by a linear momentum $\mathbf{k}$. For this reason, we are interested in those $|f\rangle$ states that after a time t_∞ evolve to asymptotically free states with well-defined momentum $\mathbf{k}$, namely $|\psi_{Na}^{f}\rangle = U_{Na}(0, t_\infty)|\mathbf{k}\rangle$, where $U_{Na}(0, t_\infty)$ is the quantum time-evolution operator.

In this evolution we assume that (i) no Na–He exciplexes are formed during the desorption process, and (ii) the helium does not induce relaxation of the excited adatoms. These assumptions, which are justified *a posteriori* by the experiments discussed below, imply that all the states accessible in the course of the excitation evolve to free 4s states of Na. This ensures that the free 4s states of Na, $|\mathbf{k}\rangle$, represent a complete basis. Introducing these states into eqn (6) we obtain

$$\begin{aligned} I(\omega,\mathbf{k}) &= \sum_n |\langle\mathbf{k}|U_{Na}(t_\infty,0)|n\rangle|^2 \\ &\quad \times |\langle n|\psi_{Na}^{gs}\rangle|^2\delta[\omega - (\omega_n - \omega_{gs})]. \end{aligned} \quad (8)$$

Integrating eqn (8) over ω one obtains the Na probability density in momentum space after the desorption process

$$I(\mathbf{k}) = \int d\omega I(\omega,\mathbf{k}) = |\langle\mathbf{k}|U_{Na}(t_\infty,0)|\psi_{Na}^{gs}\rangle|^2 = |\psi(\mathbf{k},t_\infty)|^2, \quad (9)$$

which is a measured observable in our experiments. It is worth noting that the evolution defined by $U(0, t_\infty)$ describes the processes that follow the optical excitation. Hence, at this point the FC approximation is no longer applicable and the helium density is allowed to evolve dynamically.

C. 1D exploratory calculations

To obtain the dynamical evolution, we have to solve the coupled 3D time-dependent system

$$\begin{aligned} i\hbar\frac{\partial}{\partial t}\Psi_{He}(t,\mathbf{r}) &= H_{He}^{4s}(t)\Psi_{He}(t,\mathbf{r}) \\ i\hbar\frac{\partial}{\partial t}\psi_{Na}(t,\mathbf{r}) &= H_{Na}^{4s}(t)\psi_{Na}(t,\mathbf{r}) \end{aligned} \quad (10)$$

from $t = 0$ to t_∞, using as the initial condition the 3s ground state for both the helium and the Na nuclear wave functions.

Before attempting the solution of eqn (10), we have carried out an exploratory 1D evolution. Firstly, we have solved eqn (2) by means of imaginary time methods—see *e.g.* ref. 36 and 37 for details—obtaining the 3D structure of the ground state of a Na@^{4}He$_{1000}$ droplet (shown in the top left panel of Fig. 12). Secondly, keeping the helium density frozen, we have let the Na wave function evolve in the resulting mean field potential along the symmetry axis, z, defined by the center-of-mass of the helium droplet and the sodium atom. Since the electronic excitation is assumed to be instantaneous in the FC approximation, the calculation starts from the Na wave function corresponding to the ground state of the $V_{\rm Na}^{\rm 3s}$ potential, which next evolves in the $V_{\rm Na}^{\rm 4s}$ potential shown in Fig. 1. We solve the Schrödinger equation for Na in a regular mesh using a predictor-corrector algorithm,[39] whose first time steps are provided by the outcome of a fourth-order Runge–Kutta algorithm. We have found that the Na atom reaches a quasi-free motion regime after about 1 ps. Since the helium density is not allowed to evolve, the very large mass of the helium droplet causes that all the potential energy deposited into the system during the excitation is converted into kinetic energy of the Na atom. This is in clear disagreement with the experimental results discussed below that show that a significant amount of energy is transferred to the helium droplet. The 1D calculation is nonetheless useful as it helps to identify limitations of the approach and it enables us to determine time and space scales for the full 3D simulations.

Due to the highly repulsive nature of the $V_{\rm Na}^{\rm 4s}$ potential, the Na atom leaves the droplet very quickly and attains a high mean asymptotic velocity of $\sim$650 m s^{-1}. As a result of the high velocity, fast oscillations appear in the Na wave function as shown in Fig. 2. In order to reproduce these high frequency oscillations the use of a very fine spatial mesh is mandatory. This makes a full 3D evolution computationally unaffordable. Fortunately, both the probability density and the velocity field of Na are smooth functions which makes it possible to describe the full 3D dynamics of the Na atom with quantum trajectories, an approach that uses positions and velocities instead of complex wave functions. This allows us to use a hybrid calculation scheme in which we compute the helium wave function in a mesh using standard methods for partial

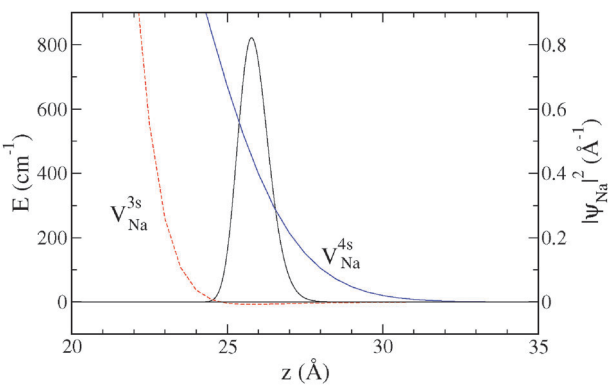

Fig. 1 Na initial probability density (thick solid line) used in the 1D calculation and the 3s ground state (dashed line) and 4s excited state (solid line) mean-field potentials. The origin corresponds to the center-of-mass of the helium droplet.

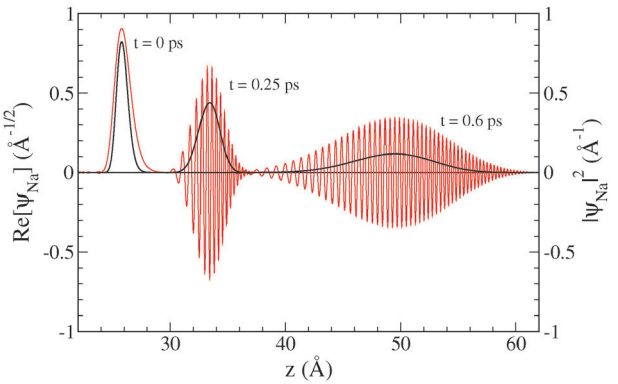

Fig. 2 Real part of the Na wave function in the 1D calculation at t = 0, 0.25, and 0.6 ps. Also shown are the probability density distributions (thick solid lines).

differential equations,[39] while the evolution of the Na atom is solved using Bohmian dynamics[21,22] as indicated below. We mention the existence of other hybrid simulations for the description of the dynamics of doped helium droplets.[40–44]

D. Bohmian trajectories for the impurity dynamics

The equation of motion for the Na trajectories $\mathbf{R}(t, \mathbf{r})$ is derived as follows.[22,24–26] We begin with writing the Na wave function in its polar form $\psi_{\rm Na}(t,\mathbf{r}) = \sqrt{\mathscr{R}(t,\mathbf{r})}e^{iS(t,\mathbf{r})/\hbar}$, where $\mathscr{R}(t, \mathbf{r})$ is the probability density and $S(t, \mathbf{r})$ is the phase in units of $\hbar$. $S(t, \mathbf{r})$ is also known as the velocity potential since the velocity field is defined as $\mathbf{v}(t, \mathbf{r}) = \nabla S(t, \mathbf{r})/m_{\rm Na}$. Splitting the Na time-dependent Schrödinger equation into its real and imaginary parts, we obtain a continuity equation for the probability density coupled to a Hamilton–Jacobi (HJ) equation for the phase

$$-\frac{\partial \mathscr{R}(t,\mathbf{r})}{\partial t} = \nabla\cdot\mathbf{j}(t,\mathbf{r})$$

$$-\frac{\partial S(t,\mathbf{r})}{\partial t} = \frac{1}{2}m_{\rm Na}|\mathbf{v}(t,\mathbf{r})|^2 + Q(t,\mathbf{r}) + V_{\rm Na}^{\rm 4s}(t,\mathbf{r}), \qquad (11)$$

where $\mathbf{j}(t, \mathbf{r}) = \mathscr{R}(t, \mathbf{r})\mathbf{v}(t, \mathbf{r})$ is the current density and

$$Q(t,\mathbf{r}) = -\frac{\hbar^2}{2m_{\rm Na}}\frac{\Delta\sqrt{\mathscr{R}(t,\mathbf{r})}}{\sqrt{\mathscr{R}(t,\mathbf{r})}} \qquad (12)$$

is the so-called quantum potential.

Eqn (11) have been solved as follows. Writing the density and the current density at time t as an histogram of M test particles with trajectories $\{\mathbf{R}_i(t)\}_{i=1}^{M}$, where $\mathbf{R}_i(t) = \mathbf{R}(t, \mathbf{r}_i)$ and $\mathbf{R}_i(0) = \mathbf{r}_i$, we get

$$\mathscr{R}(t,\mathbf{r}) = \lim_{M\to\infty}\frac{1}{M}\sum_{i=1}^{M}\delta[\mathbf{r}-\mathbf{R}_i(t)]$$

$$\mathbf{j}(t,\mathbf{r}) = \lim_{M\to\infty}\frac{1}{M}\sum_{i=1}^{M}\mathbf{v}[\mathbf{R}_i(t)]\delta[\mathbf{r}-\mathbf{R}_i(t)]. \qquad (13)$$

The continuity equation is automatically fulfilled if $\boldsymbol{R}_i(t) = \mathbf{v}[\mathbf{R}_i(t)]$, *i.e.*, if the change in time of the position of the test particle is just the velocity field evaluated at the position of that test particle. The equation of motion obeyed by the

velocity field—and thus the equation for the trajectories—is obtained by taking the gradient of the HJ equation and rewriting it in the Lagrangian reference frame ($d/dt = \partial/\partial t + \mathbf{v}\cdot\nabla$). One then obtains the quantum Newton equation

$$m_{Na}\ddot{\mathbf{R}}_i(t) = -\nabla[Q(t, \mathbf{r}) + V^{4s}_{Na}(t, \mathbf{r})]|_{\mathbf{r} = \mathbf{R}_i(t)}. \quad (14)$$

In this way, both helium wave function and Na trajectories are computed consistently at each time step of 10^{-4} ps using a fourth-order Runge–Kutta algorithm. The quantum potential $Q(t, \mathbf{r})$ is computed using the histogram of the test particles as probability density in a regular mesh with a spatial resolution of 0.35 Å, and 13-points formulas for the derivatives involved. Simultaneously, the helium wave function is evolved with a fourth-order Runge–Kutta algorithm, using as the initial condition the 3s ground state helium density and a set of $M = 200\,000$ positions randomly generated from the 3s ground state Na probability density. The system is solved up to $t_\infty = 5$ ps ($t_\infty = 3$ ps in the case of Li), when the test particles are far enough from the droplet to follow quasi-free trajectories at constant velocity. Note that this time is five times longer than that of the 1D exploratory calculation with the frozen helium density.

E. Practical evaluation of the Fermi Golden Rule

To complete the evaluation of the GR expression eqn (8), we have resorted to a semiclassical approximation for the H^{4s}_{Na} hamiltonian for obtaining the dipole absorption spectrum of atomic impurities:[36] the kinetic term is neglected and the hamiltonian is replaced by the potential energy, $H^{4s}_{Na}(0) \rightarrow V^{4s}_{Na}(0, \mathbf{r})$. Thus, its eigenstates are those of the position operator, $|n\rangle \rightarrow |\mathbf{r}\rangle$, and its eigenvalues those of the potential energy surface evaluated at $\mathbf{r}$, thus $\hbar\omega_n \rightarrow V_{4s}(\mathbf{r})$ and the sum over states becomes an integral $\sum_n \rightarrow \int d\mathbf{r}$, allowing us to write

$$I(\omega, \mathbf{k}) = \int d\mathbf{r} |\langle \mathbf{k}|U_{Na}(t_\infty, 0)|\mathbf{r}\rangle|^2 \times |\langle \mathbf{r}|\psi^{gs}_{Na}\rangle|^2 \delta[\hbar\omega - (V_{4s}(\mathbf{r}) - \hbar\omega_{gs})]. \quad (15)$$

Within the quantum trajectory description for the Na atom, the probability $|\langle \mathbf{k}|U_{Na}(t_\infty, 0)|\mathbf{r}\rangle|^2$ is written as $\delta[\mathbf{k} - \mathbf{K}(t_\infty, \mathbf{r})]$, where $\mathbf{K}(t_\infty, \mathbf{r})$ is the momentum at t_∞ of the trajectory with initial position $\mathbf{r}$ at $t = 0$. Since Na moves at t_∞ as a free particle, we can safely consider $\hbar\mathbf{K}(t_\infty, \mathbf{r}) = m_{Na}\dot{\mathbf{R}}(t_\infty, \mathbf{r})$. Using the definition in eqn (13) for the Na probability density, eqn (15) is then computed as

$$I(\omega, \mathbf{k}) = \frac{1}{M}\sum_{i=1}^{M} \delta[\hbar\mathbf{k} - m_{Na}\dot{\mathbf{R}}_i(t_\infty)] \times \delta\{\hbar\omega - [V^{4s}_{Na}(0, \mathbf{R}_i(0)) - \hbar\omega_{gs}]\}. \quad (16)$$

The semiclassical approximation incorporates the trajectories in a natural way by correlating along each trajectory its initial potential energy with its asymptotic linear momentum. Note that though the evaluation of the GR is semiclassical, the trajectories are quantum-mechanically determined.

Incorporating shape fluctuations of the helium droplet around the impurity has proved to be crucial for achieving a quantitative description of processes involving impurities in helium, as they substantially contribute to the broadening of observables.[14,45,46] For this reason, we have included the effect of fluctuations in the evaluation of eqn (16) *a posteriori*, *i.e.*, after the time evolution, using the DF-sampling method, as shown in the Appendix B, eqn (B5). Inclusion of the density fluctuations mainly affects the width of physical observables such as the excitation spectrum and the velocity and kinetic energy distributions of the desorbed atoms.

We want to stress that the transition probability $w_{i\rightarrow f}$ contains all the physical information that can be experimentally determined. In point of fact, (i) by integrating over $\mathbf{k}$ we obtain the excitation spectrum, as seen in eqn (7); (ii) by fixing the excitation energy ω, we obtain the distribution over momentum $\mathbf{k}$, corresponding to the velocity distribution of the desorbed atom; and (iii) by the change of variable $E_k = \hbar^2k^2/2m_{Na}$ the kinetic energy distribution is obtained. The explicit expressions used to compute these quantities are reported in Appendix B.

IV. Results

A. Excitation spectra

To investigate the desorption dynamics of sodium and lithium atoms from the surface of helium nanodroplets, the alkali atoms have been excited to their nominal 4s and 3s states, respectively. The corresponding excitation spectra are shown in Fig. 3 and 4. The spectra of the two lithium isotopes, ^{6}Li and ^{7}Li, have been recorded individually by gating the detector at the appropriate arrival time of these ions. It should be noted that only bare sodium and lithium ions have been observed and that no complexes with helium were detected, as was explicitly checked by time-of-flight mass spectrometry. This implies that the excitation spectra reported in Fig. 3 and 4 correspond to absorption spectra, which allows for a direct comparison between the experimental and theoretical spectra. The spectra are all characterized by a broad absorption band that is blue-shifted with respect to the transition in the free atom. The 4s ← 3s transition of sodium-doped droplets has been discussed in detail before and the large blue-shift has been attributed to the repulsive character of the 4s effective potential,[17] see also Fig. 1.

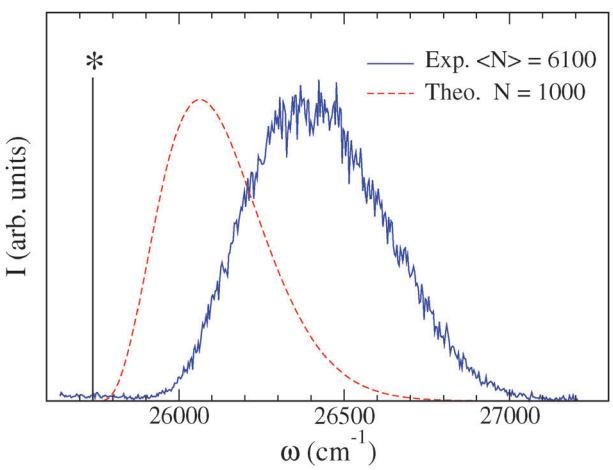

Fig. 3 Theoretical and experimental excitation spectrum of the 4s ← 3s transition of Na on ^4He_N droplets. The top-starred vertical line corresponds to the free atom transition.[48]

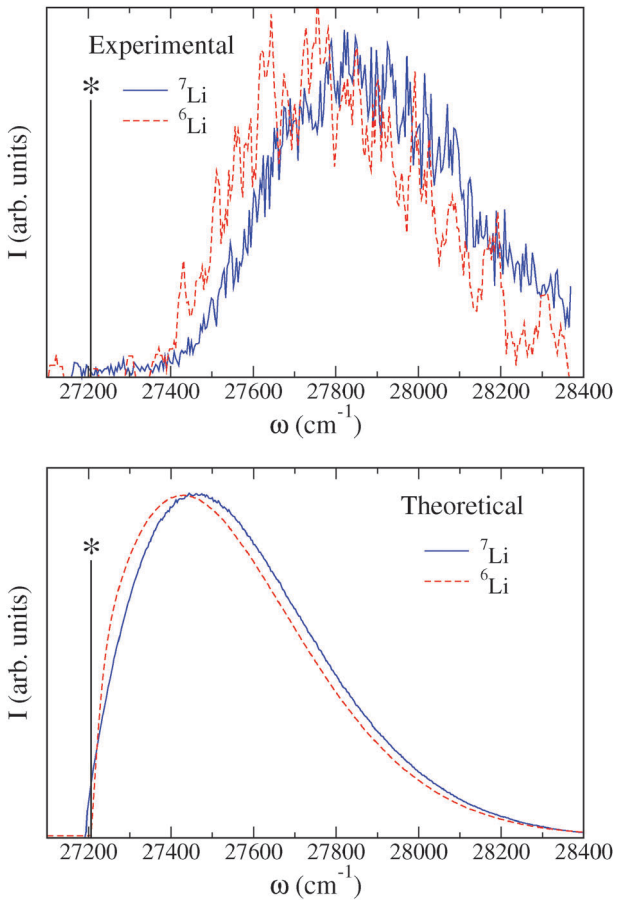

Fig. 4 Top panel: Experimental excitation spectrum of the 3s ← 2s transition for Li attached to helium droplets consisting on average of 6100 atoms. Bottom panel: Corresponding theoretical spectrum for Li@^{4}He$_{1000}$. The top-starred vertical line corresponds to the free atom transition.[48]

The absorption spectrum of the 4s ← 3s transition for the Na@^{4}He$_{1000}$ system has been calculated taking explicitly into account dimple fluctuations using the atomic-like DFT sampling technique, eqn (B7). The width of the experimental spectrum, 400 cm^{-1}, is well reproduced by the calculations which yield a value of 370 cm^{-1}. In contrast, the spectral shift, which is droplet size dependent and amounts to 570 cm^{-1} for droplets consisting on average of 1700 helium atoms, is somewhat underestimated by the calculation that yields 350 cm^{-1} for $N = 1000$.

We would like to mention that although the absorption spectra of Na[17] and other impurities[13,36] calculated by semi-classical methods yield at times quantitative agreement with the experimental spectra, the DFT sampling method employed here constitutes a consistent framework that is able to reproduce the basic spectral features both in droplets and bulk helium.[14,45–47] It is evident that since the helium–helium correlations are described in a semiclassical way, the method still needs some improvements. In spite of this limitation, it is the only workable method for incorporating density fluctuations within the DFT scheme, and it is for this reason that we use it in this investigation.

Inspection of the spectra for the two lithium isotopes shown in Fig. 4 reveals that they are very similar but that the

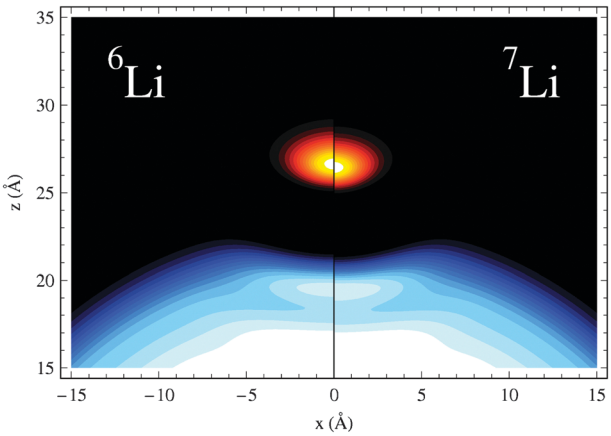

Fig. 5 Dimple structure of ^{6}Li@^{4}He$_{1000}$ (left) and ^{7}Li@^{4}He$_{1000}$ (right) droplets. The probability density distribution of the dopant is also shown.

spectrum of ^{6}Li is slightly less blue-shifted than that of ^{7}Li. Solving the equivalent of eqn (2) for both isotopes indicates that this difference is related to the ground state structure: as can be seen in Fig. 5 the lighter ^{6}Li isotope generates a less pronounced dimple structure and is more delocalized than the heavier ^{7}Li isotope. As a result, the lighter isotope probes the excited state potential at larger distances corresponding to lower energies. It is interesting to note that similar zero point motion effects have been observed for Li on ^{3}He and ^{4}He droplets.[45] The calculations accurately reproduce the width of the absorption line (540 cm^{-1} in the calculations *vs.* 530 cm^{-1} in the experiments) and the isotopic shift (relative difference of 13% in the calculations and 15% in the experiments). As discussed above, the calculations somewhat underestimate the absolute blue-shift of the spectrum. We would like to point out that since the helium–lithium interaction is isotope-independent, all the differences found in the ground state structure—and thus in the excitation spectra—arise from the kinetic energy term in eqn (2) for Li. It is thus a pure quantum effect (zero point motion) and consequently cannot be reproduced by the calculations if the impurity is included as an external field.

B. Photoelectron spectra

The desorption efficiency and the helium-induced relaxation of excited alkali atoms have been investigated using photoelectron spectroscopy. Fig. 6 shows the photoelectron spectrum obtained following excitation of sodium-doped helium nanodroplets at a frequency of 26 316 cm^{-1}, corresponding to the maximum of the absorption band. The spectrum is characterized by a strong peak at low photoelectron kinetic energy and a much weaker peak at higher energies. Based on the photon energy and the ionization potential of sodium,[48] the low energy peak can be readily assigned to gas phase sodium atoms in the 3p state. The peak at high energy corresponds to free sodium in the 4s state. Since the spectrum reveals no other peaks which could be assigned to excited sodium atoms attached to the helium droplets,[16] we conclude that all excited atoms desorb from the droplets on the timescale of the laser pulse.

The photoelectron spectrum gives the impression that the helium induces a strong relaxation of the excited sodium, since

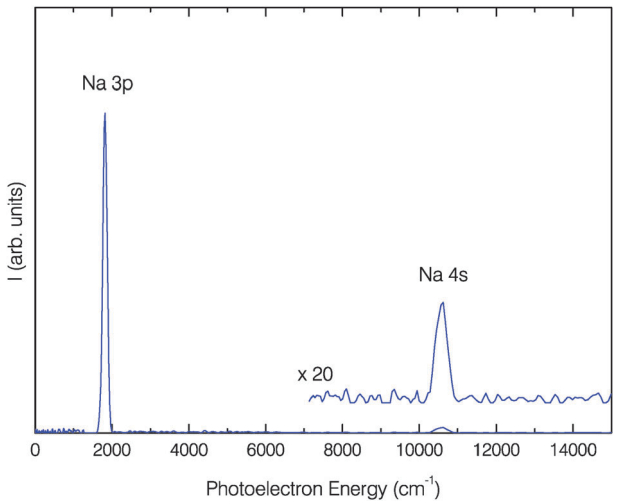

Fig. 6 Photoelectron spectrum recorded following photoexcitation of sodium-doped helium droplets at 26 316 cm^{-1}.

the majority of the sodium atoms are found to reside in the 3p state and not in the initially excited 4s state. However, when interpreting the photoelectron spectrum one has to take into account that the 4s state has a short radiative lifetime[48] and that the ionization cross sections depend strongly on the excited state of the sodium atom.[49,50] Unfortunately, it is not possible to address this issue by recording the corresponding photoelectron spectrum of free sodium, as the 4s ← 3s transition is dipole forbidden for one-photon excitation in the free atom. The photoelectron spectrum therefore has been simulated using a rate equation approach. The model used is graphically depicted in Fig. 7. Following excitation of the surface bound sodium atoms to the nominal 4s state they desorb from the helium droplets. The free atoms decay by spontaneous emission to lower lying states. This process is characterized by the Einstein coefficients $A_{4s\rightarrow 3p}$ and $A_{3p\rightarrow 3s}$.[48] During the laser pulse the excited atoms are ionized with an efficiency that is determined by the state specific ionization cross sections σ_{4s} and σ_{3p}[49,50] and the laser intensity. To model the photoelectron spectra we now assume that no relaxation is induced by the helium and that the atoms desorb instantaneously from the droplets. This latter assumption is justified

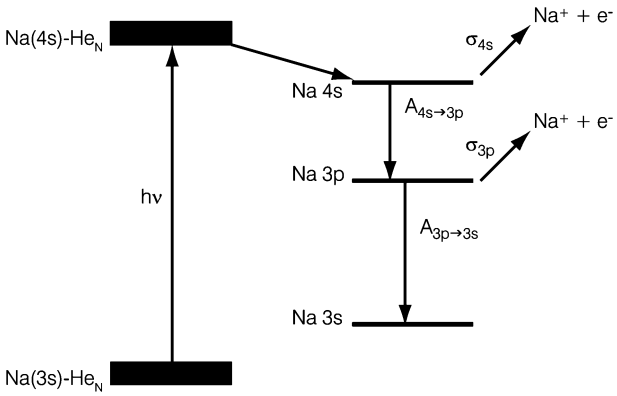

Fig. 7 Energy level diagram displaying the relation and excitation processes taking place after excitation of sodium-doped helium droplets *via* the 4s ← 3s transition, see text for details.

Table 1 Experimental and calculated relative intensities of the photoelectron peaks following excitation of sodium-doped helium droplets *via* the 4s ← 3s transition

State	Experiment	Model
3p	0.96(1)	0.89(4)
4s	0.04(1)	0.11(4)

by the fact that the radiative lifetime and the interaction time of the free atoms with the light pulse are much longer than the desorption time of the excited atoms, *vide infra*. It should be noted that with these assumptions the calculated photoelectron spectrum corresponds to that of a free sodium atom resonantly ionized by a 1 + 1 photon excitation process *via* the 4s state. The set of coupled equations describing the ionization of the free sodium atoms has been solved numerically assuming that the 11 ns laser pulse can be approximated by a Gaussian distribution. The uncertainties of the various constants used, as well as laser power fluctuations have been included in the simulations to determine the uncertainty of the relative intensities in the calculated photoelectron spectrum.

The theoretically and experimentally determined intensity ratios are reported in Table 1. As can be seen from the table, the large intensity of the 3p state is well reproduced by the calculations. This signifies that the 3p state is mainly populated by spontaneous emission of 4s excited sodium atoms during the laser pulse. The small discrepancy between the theoretical and experimental results might be attributed to the large uncertainty associated with the σ_{4s} ionization cross section, which is close to its minimum at the excitation frequency used. Alternatively, it might indicate that some helium-induced relaxation takes places during the desorption process. In view of the good agreement between experiment and model calculations, we assume that all sodium atoms leave the helium droplets in the initially excited 4s state. Although no photoelectron spectra have been recorded for lithium, we presume that they behave similar to sodium, *i.e.* all the excited lithium atoms desorb from the droplets without undergoing helium-induced relaxation.

C. Velocity and kinetic energy distributions

To obtain insight into the desorption dynamics the velocity distributions of the desorbed atoms have been determined. To this end ion images have been recorded at several frequencies within the absorption bands. Fig. 8 shows two ion images of sodium that have been recorded following excitation at the low and high frequency end of the 4s ← 3s excitation spectrum. Both images are characterized by a strong anisotropic angular and radial distribution, indicating that the desorbing atoms leave the droplets with a well-defined velocity distribution. By performing an inverse Abel transform to these images the speed distribution and the angular anisotropy parameter β have been determined.

The resulting speed distributions, which are also shown in Fig. 8, are found to depend strongly on the excitation frequency. While excitation at 26 100 cm^{-1} yields sodium atoms with a most probable speed of 440 m s^{-1}, excitation at 26 600 cm^{-1} yields significant faster sodium atoms having speeds of 695 m s^{-1}. Whereas the speed distributions depend on the

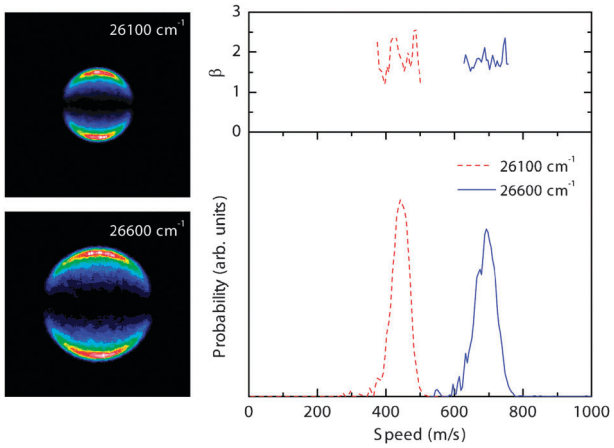

Fig. 8 (left) Ion images of sodium atoms desorbed from the surface of helium droplets following excitation at two frequencies within the 4s ← 3s resonance. The polarization of excitation laser is vertical with respect to the images. (right) Speed distributions and anisotropy parameters derived from the ion images.

Table 2 Characteristics of the experimental and theoretical kinetic energy distributions of the desorbed alkali atoms, see text for details

	Experiment					Theory	
Atom	ω_0/cm^{-1}	η	η_Δ	β	m_{eff}/amu	ω_0/cm^{-1} 48	η
^{6}Li	27 218(6)	0.743(6)	0.042(6)	1.73(6)	17.4	27 206	0.802(8)
^{7}Li	27 222(3)	0.687(3)	0.040(2)	1.79(3)	15.4	27 206	0.756(8)
^{23}Na	25 743(4)	0.516(4)	0.038(3)	1.81(6)	24.5	25 740	0.583(9)

excitation frequency, the angular distributions do not show such dependence. The anisotropy parameter β is found to be independent of the velocity of the desorbing sodium atoms and has a mean value of 1.81 ± 0.06. Similar values for the anisotropy parameter are found for desorbed lithium atoms, see Table 2. It should be noted that the speed distributions and the values for the anisotropy parameters are found to be independent of the helium droplet size. This can be attributed to the local character of the interaction of the alkali atom with the helium droplet.

The values of the anisotropy parameter found in the experiments are close to that expected for the parallel $(n+1)$s ← ns transitions. As discussed before, the small deviation from this value might be due to helium-induced configuration mixing. Recently, Callegari and Ancilotto proposed a method to calculate the interaction potentials of alkali atoms on helium nanodroplets that explicitly takes into account configuration mixing.[51] Using the expansion coefficients determined by this method,[52] evaluation of eqn (21) yields a value of $\beta = 1.99$ for the anisotropy parameter. Evidently, configuration mixing cannot account for the experimentally observed anisotropy. A reduction of the anisotropy parameter also can result if the rotational period of the helium droplets is comparable to the time scale of desorption.[53] Even though not much is known about the rotation of helium droplets, it is to be expected that the rotational period depends on the size of the droplets. Since the anisotropy parameter is identical for all three adatoms and does not depend on the velocity of the desorbed atoms nor on the helium droplet size, it is highly unlikely that droplet rotation is the cause for the reduced anisotropy parameter. It is more likely that density fluctuations of the helium in the proximity of the alkali atoms during the desorption process lead to off-axis motion of the alkali atom. As we show in Appendix A, the deformations induced by the helium fluctuations can indeed result in a decrease of the anisotropy value. An estimation of the order of magnitude of that decrease demands an explicit calculation of the electronic configurations, which is beyond the scope of this work.

In order to establish a relation between the kinetic energy of the desorbing atoms and the excitation frequency, the speed distributions have been transformed into kinetic energy distributions, see Fig. 9, and their average value and standard deviation have been determined. Fig. 10 shows the average kinetic energy of desorbed sodium atoms as a function of excitation frequency, while Fig. 11 shows those for the two lithium isotopes. For all three impurities the average kinetic energy shows a linear dependence on the excitation frequency. The data points therefore have been fitted to the following expression:

$$\langle E_{kin} \rangle = \eta(\hbar\omega - \hbar\omega_0) \quad (17)$$

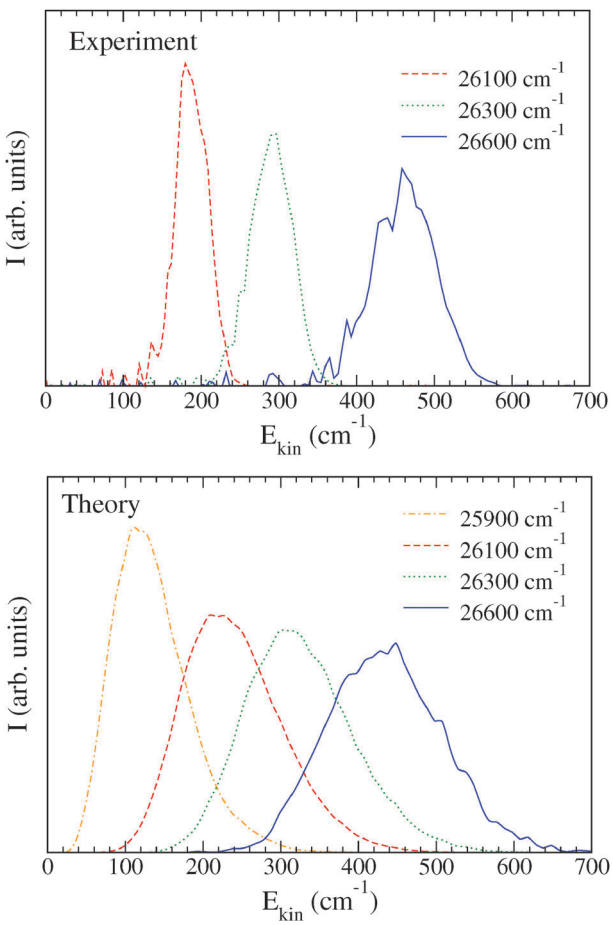

Fig. 9 Experimental (top panel) and theoretical (bottom panel) normalized kinetic energy distributions of desorbed Na atoms following excitation at different energies.

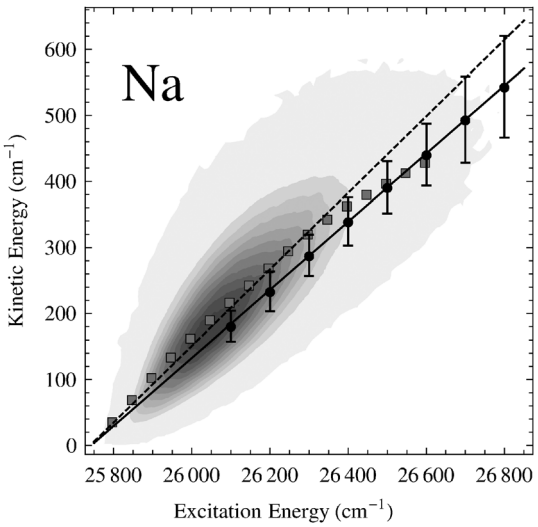

Fig. 10 $I(\omega, E_k)$ distribution for Na atoms. Squares: theoretical mean kinetic energy. Dashed line: linear fit to the theoretical data up to an excitation energy of 26 400 cm^{-1}.[54] Dots: experimental mean kinetic energy. Bars: experimental standard deviation of the kinetic energy distributions. Solid line: linear fit to the experimental data.

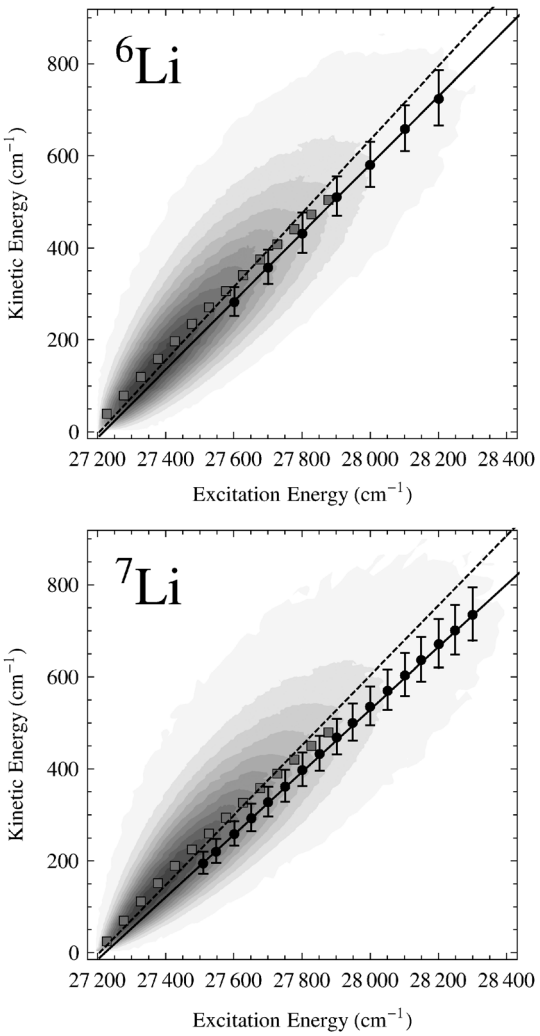

Fig. 11 Same as Fig. 10 for Li. In this case, all the points shown have been included in the fit of the theoretical data.

where $\hbar\omega_0$ corresponds to the excitation energy yielding alkali atoms with zero kinetic energy, while η is a proportionality constant. The constants derived from the fits are reported in Table 2. The values of ω_0 are very close to the transition frequencies of the free atoms, *i.e.*, 25 740 cm^{-1} and 27 206 cm^{-1} for sodium and lithium, respectively.[48] The good agreement between these values indicates that the proportionality constant η can be interpreted as the fraction of the available energy that is converted into kinetic energy of the desorbing alkali atom. The values of η as determined in the experiment depend not only on the type of alkali atom but also on its mass, see Table 2. The lighter the atom, the larger the value of η and thus the larger the fraction of available energy that is carried away by the departing atom. The standard deviation of the kinetic energy distribution, indicated by the bars in Fig. 10 and 11, also shows a linear dependence on excitation frequency and therefore has been fitted to the same functional form as the average kinetic energy. In contrast to the average kinetic energy, the proportionality constant for the standard deviation, η_Δ, does not depend on the atom nor its mass, see Table 2.

More insight into the desorption process can be gained from the calculations. As can be seen in Fig. 1, excitation of Na to the 4s state leads to a highly repulsive interaction between the sodium atom and the droplet which triggers the desorption of the impurity. Fig. 12 shows the evolution of the Na@^{4}He$_{1000}$ system after excitation of the sodium atom. Inspection of this figure reveals that the desorption of the sodium atom is accompanied by the creation of density waves in the helium droplet. This indicates that a fraction of the energy deposited in the system by the optical excitation is transferred to the helium cluster. It can be seen from the figure that after $\sim$1.5 ps the Na atom has left the droplet surface and the helium starts filling the dimple. The calculations are stopped after 5 ps, when the sodium atom has reached an asymptotic mean velocity of 510 m s^{-1}. During the 5 ps time propagation, the position of the center-of-mass of the droplet experiences a minute displacement of 0.1 Å. Assuming a constant motion, the translational energy of the droplet is calculated to be 0.7 cm^{-1}, indicating that most of the energy transferred to the helium cluster is converted into internal energy.

In the calculations, the GR is evaluated according to eqn (B1) using the initial position and final velocities of the Na test particles as input. This expression gives direct access to the final velocity distributions of the desorbed alkali atoms. To obtain a correlation between the asymptotic kinetic energy distributions and the excitation energy, the GR is evaluated using eqn (B2). The results of the calculations are compared with experimental kinetic energy distributions in Fig. 9. It can be seen that as the excitation energy increases, the kinetic energy distributions shift to higher energies and broaden. While these trends are well reproduced by the calculations, the widths of the distributions are somewhat overestimated. This can be attributed to the semiclassical method used to simulate the density fluctuations, as discussed before.

The full $I(\omega, E_k)$ distribution calculated for Na is shown in Fig. 10 by a false color representation. The average kinetic

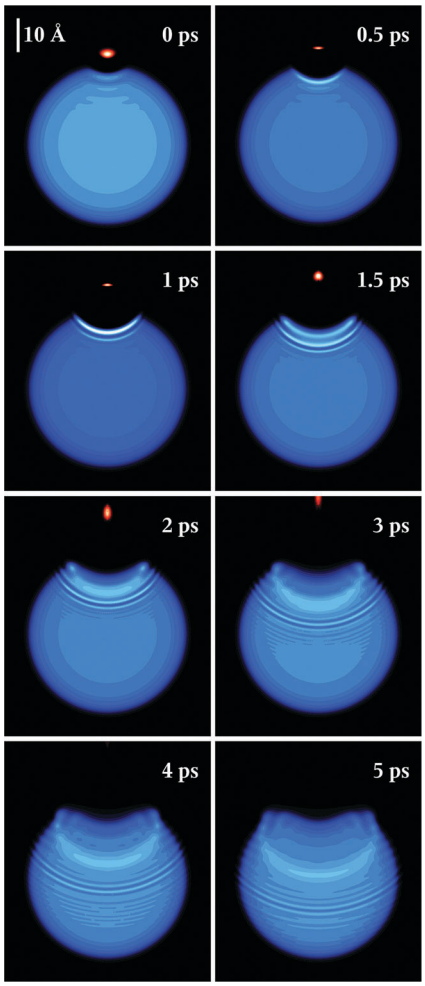

Fig. 12 Evolution of the Na@^{4}He$_{1000}$ complex after excitation.

energy of the desorbed sodium atoms derived from this distribution at selected excitation energies is also presented in this figure. The calculations show a strong correlation between the mean kinetic energy and the excitation energy, in agreement with experiments. A linear fit to the theoretical data points yields a slope 0.58 which compares well to the experimental value of 0.52. It is important to point out that it is essential to take into account the density fluctuations in order to achieve a good agreement with experiment. If the density fluctuations are not included in the calculations a slope of 0.76 is obtained. This leads to the conclusion that the density fluctuations are responsible for the absorption of a large part of the energy deposited in the system by the electronic excitation.[40] Calculations for the smaller Na@^{4}He$_{500}$ complex yield results similar to those for Na@^{4}He$_{1000}$. This size independence is in agreement with experiment, and can be attributed to the local character of the interaction of the alkali atom with the helium droplet.

The calculations reveal that lithium behaves very similar to sodium, although there are some differences. Due to the lighter mass and a less pronounced dimple, Li atoms desorb faster from the droplets than Na atoms and reach the asymptotic free regime already after ~3 ps. Their asymptotic mean velocities are significantly higher than for sodium and are slightly different for the two Li isotopes, ^{6}Li being faster than ^{7}Li. The $I(\omega, E_k)$ distributions for Li are shown in Fig. 11 together with the experimental data. Also in this case the calculations display a similar correlation between the mean kinetic energy of the desorbed atom and the excitation energy. In agreement with experiment, see Table 2, slightly different slopes for the two isotopes are found, 0.80 for ^{6}Li and 0.76 for ^{7}Li, confirming the mass-dependent nature of the process.

As a final comment, we want to point out that while the experimental mean kinetic energies vary essentially linearly with excitation energy, the theoretical values show some non-linearity, especially at higher excitation energies. We have found that the variation becomes more linear at these energies if we do not include helium density fluctuations. This indicates that at least part of the non-linearity arises from the way fluctuations are handled.

D. Helium density waves

Whereas the experiments provide only information on the desorbing alkali atom, the calculations also provide insight into the dynamics of the helium droplet upon excitation of the adsorbed atom. As an example, in Fig. 13 the helium density profile of a Li@^{4}He$_{1000}$ droplet along the symmetry axis is represented as a function of time. This figure, together with Fig. 12 for Na, gives a pictorial yet quantitative representation of the dynamics triggered by the excitation of the alkali atom. In particular, they show the dramatic changes in the droplet density caused by the excitation and subsequent desorption of the impurity.

To establish the nature of the helium density waves created by the excitation, we concentrate on the simulations for Na, as

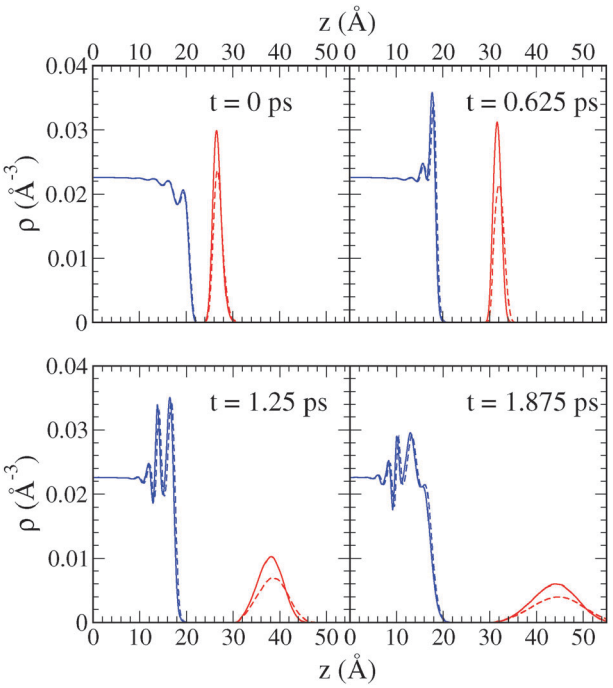

Fig. 13 Helium density profiles and Li probability density distributions (Gaussian-like profiles) showing the dynamical desorption of Li isotopes along the symmetry axis. Dashed lines, ^{6}Li. Solid lines, ^{7}Li.

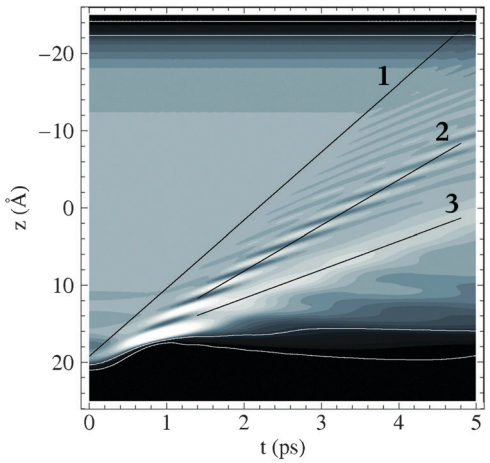

Fig. 14 Evolution of the helium density profile of the Na@^{4}He$_{1000}$ system along the symmetry axis. Three supersonic fronts are identified and labelled by roman numbers. Equidensity lines corresponding to 0.5 and 0.1 times the helium saturation density, 0.0218 Å^{-3}, are shown in white.

they last for longer times. Fig. 14 shows the evolution of the helium density profile of a Na-doped ^{4}He$_{1000}$ droplet during the first 5 ps. Initially, the droplet extends along the z (symmetry) axis from about 21 to −25 Å, and the Na atom is located in a dimple at the surface. Excitation of the sodium to the 4s state causes the dimple first to deepen due the highly repulsive nature of the He–Na 4s interaction. The associated compression of the helium last up to ∼1 ps, as shown in the figure. Following this compression, the helium surface bounces back and the dimple starts being filled. The more distant part of the droplet at ∼−25 Å remains unperturbed and at rest, indicating that energy deposited in the droplet leads almost exclusively to the excitation of its internal degrees of freedom and not to a translational motion of the droplet as a whole.

Fig. 12–14 all reveal that excitation of the alkali atom launches highly non-linear density waves into the helium droplet. This becomes even clearer in Fig. 15 which shows the density variations along the symmetry axis at different

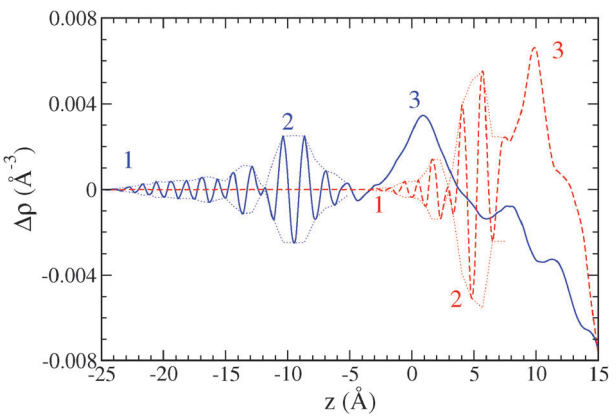

Fig. 15 Difference between the density profile and the initial density along the symmetry axis, $\Delta\rho \equiv \rho(t, z) - \rho(0, z)$, for t = 2.5 ps (dashed lines) and t = 5 ps (solid lines). The envelope wave of the modulated carrier waves is also shown for clarity (dotted lines). The three identified fronts are labelled as in Fig. 14.

times. The waves created by the excitation propagate in the droplet at supersonic velocities.[55] In the case of Na, see Fig. 14 and 15, the first perturbation front, labelled as 1, moves at ∼890 m s^{-1} and reaches the opposite 'edge' of the droplet in less than 5 ps. This perturbation generates carrier waves with a phase velocity between 300 and 370 m s^{-1}, modulated by supersonic envelope fronts with growing intensity. The ones with highest intensity, labelled as 2, have a group velocity of ∼590 m s^{-1}. The origin of this modulation can be traced back to the original structure of the droplet, being an 'echo' of the solvation shells around the impurity in its ground state. Next, a high intensity wave appears travelling at ∼370 m s^{-1} (labelled as 3), which generates secondary waves propagating backwards. A closer analysis of this wave has allowed us to identify it with a solitary wave, or soliton. Indeed, it can be seen from Fig. 14 and 15 that it always corresponds to the maximum intensity of the travelling wave.

We have found similar density waves in the case of Li, for which we recall that the evolution is stopped after 3 ps. This time is long enough to establish that the first perturbation front moves at about 750 m s^{-1} for both isotopes. This speed is lower than in the case of sodium which might be attributed to the smaller amount of energy that is deposited into the droplet. Waves 2 and 3 develop as well, although they are not so clearly visible and their velocities cannot be determined with confidence.

To our knowledge, the existence of these types of travelling waves has not been disclosed before. They bear some similarities with the waves produced in liquid helium by the de-excitation of electron bubbles.[56,57] These waves have been identified with shock waves in ref. 56, but with no clear justification for this statement.

V. Further remarks

The most pertinent result of this study is undoubtedly the fact that the asymptotic kinetic energy of the desorbing alkali atoms scales linearly with the excitation energy. Both experiment and theory find that the amount of energy carried away by the desorbing alkali atom depends not only on the atom but also on its mass. In particular, the larger the mass of the impurity, the larger the amount of energy deposited in the helium droplet.

Even though the calculations reproduce the experimental observations fairly well, they do not provide the physical insight required to identify the precise mechanism giving rise to the particular partitioning of the available energy between the desorbing alkali atom and the helium droplet. Rather than a limitation of the method used, this is a signature of the actual complexity of the desorption process.

Nonetheless, one would like to have some insight into the physical processes leading to the particular energy partitioning. In view of the analogy, one might consider describing the desorption of an excited alkali atom from the surface of a helium droplet as a photodissociation reaction. Various models have been put forward to describe the photodissociation of polyatomic molecules, each of them focussing on specific aspects of the process.[58] In the case of a direct dissociation *via* excitation to a repulsive state, the process is best described

by the simple impulsive model introduced by Busch and Wilson in their seminal work on the photodynamics of NO_2.[59] The basic idea of the impulsive model is that the force needed to break apart the molecule is solely directed along the axis of the dissociating bond. Under the assumption that the bond breaks promptly, the available energy is initially partitioned, by conservation of linear momentum, between the kinetic energies of the two atoms forming the bond. The kinetic energy of the atoms is subsequently partitioned between the translation, rotational and vibrational degrees of freedom of each fragment. This impulsive model might be well suited to describe the desorption of an alkali atom from the surface of a helium droplet given that excitation of the alkali atom leads to a highly repulsive interaction between the excited atom and the helium droplet, see Fig. 1, and a fast desorption of the alkali atom. The main difficulty in applying the impulsive model to the helium droplet system lies in that the alkali atom is not bound to a single helium atom but interacts with all the atoms making up the droplet. However, due to its short range character, the repulsive interaction is by far the strongest with the nearby helium atoms located at the surface of the dimple.[35] This is also born out by the calculations which reveal that predominantly these helium atoms are displaced immediately after excitation of the alkali atom, see Fig. 12. One might therefore consider reducing the problem to a pseudo-polyatomic model in which the alkali atom having a mass of m_{Ak} is considered to be bound to the helium droplet *via* a single helium moiety with an effective mass of m_{eff} that is to be determined. Assuming that the impulsive model can be applied to this strongly simplified description of the system, the kinetic energy of the desorbed alkali atom, $E_{kin}(Ak)$ is related to the available energy $\Delta\hbar\omega$ according to:

$$E_{kin}(Ak) = \frac{m_{eff}}{m_{eff} + m_{Ak}} \Delta\hbar\omega. \qquad (18)$$

The model thus yields a linear dependence of the kinetic energy on excitation frequency, as is observed in the present study. The slope is directly related to the effective mass of the helium moiety with which the excited alkali atom interacts. Since the alkali atom interacts with several helium atoms located at the surface of the dimple, we expect m_{eff} to be larger than the mass of a single helium atom. Although m_{eff} cannot be calculated *a priori*, it can be determined by fitting the experimental slope of the kinetic energy on excitation frequency, see Table 2. One finds an effective mass of $\sim$16 and $\sim$24 amu for Li and Na, respectively. This would signify that the 3s electron of Li interacts on average with 4 helium atoms, while the 4s electron of sodium interacts with 6 helium atoms. The difference in the number of interacting helium atoms is thought to reflect the difference in electron orbit radius and dimple structure.

We would like to stress here that in spite of the fact that the impulsive model offers an explanation for some of the experimental and theoretical observations, it is only an approximative description that lacks any predictive power. The effective mass required for this model can only be determined *a posteriori* from the experimental or theoretical data. Due to the approximative nature of the model this effective mass should be interpreted with care. This is exemplified by the results for the two lithium isotopes, where according to the impulsive model ^{6}Li interacts with more helium atoms than ^{7}Li, see Table 2. This contradicts the conclusion based on the difference in the excitation spectrum of the two lithium isotopes and the calculations of the ground state structure, which indicate that the lighter ^{6}Li atom is located further away from the droplet surface and consequently interacts less with the helium than the ^{7}Li atom.

As a final remark, the weak dependence of the standard deviation of the energy distributions on the alkali atom or its mass points to the helium as the source of the broadening. As seen in the calculations, helium density fluctuations cause some dispersion in the observables. Since these fluctuations are to a large extent independent of the impurity attached to the droplet, it is expected that so is the dispersion of the observables.

VI. Summary

We have carried out a combined experimental and theoretical investigation of the desorption of Na and Li alkali atoms from the surface of helium droplets following excitation *via* the $(n + 1)s \leftarrow ns$ transition. These systems are well suited to gain insight into the dynamics of this complex phenomena, since neither exciplex formation nor helium-induced relaxation of the impurity obscures the analysis of the experimental findings or its theoretical interpretation.[17] Additionally, the use of Li allows us to address the mass effect in the desorption process by making a direct comparison between the results for ^{6}Li and ^{7}Li.

The analysis of the experimental results has been carried out within a full dynamical, three dimensional approach that combines a time-dependent DFT description of the droplet with a Bohmian description of the impurity. To the best of our knowledge, this is the first time that such a theoretical framework has been developed and applied to the desorption of impurities from helium droplets.

The experiments reveal that the $(n + 1)s \leftarrow ns$ transitions of Li and Na atoms located on helium droplets are significantly blue-shifted with respect to the corresponding gas phase transitions. They furthermore disclose that excitation of the alkali atom leads in all cases to its desorption from the helium droplet and that the average kinetic energy of the desorbed atom depends linearly on the excitation energy. These observations are all reproduced by the calculations, which allows us to have confidence in theoretical observations that cannot be experimentally verified. More specifically, the calculations indicate that the energy deposited in the system by the excitation of the alkali atom leads to the creation of highly nonlinear helium density waves that propagate through the helium droplet at supersonic velocities. One of such waves could be identified as a soliton. Based on the good agreement between experiment and theory it becomes also possible to identify the main physical ingredients necessary for a quantitative description of the desorption process, namely: (i) the zero-point motion of the impurities, (ii) a full dynamical description of both the helium droplet and the impurity, and (iii) the inclusion of helium density fluctuations. These concepts have been implemented in a numerical approach that is very robust and can be applied to the description of other dynamical processes

involving atomic impurities propagating in helium droplets.[27,28,43,44,60] Addressing exciplex formation, as observed in several systems,[17,19,41,42,61–64] however, still remains a challenge from a computational point of view that will likely require a test particle description of both the impurity and the helium droplet.

Appendix A

We discuss in this Appendix the probability of an optical transition between mixed electronic orbitals. Defining the initial and final states in cylindrical symmetry as

$$\varphi_i(\theta) = \sum_{\ell=0}^{\infty} A_\ell Y_{\ell 0}(\theta)$$

$$\varphi_f(\theta) = \sum_{\ell=0}^{\infty} B_\ell Y_{\ell 0}(\theta),$$

where $Y_{\ell m}$ are the spherical harmonics of order (ℓ, m), the angular dependence of the dipolar transition probability is written as[33]

$$P_{i\to f}(\theta) = \sum_{\ell\ell'} |B_\ell|^2 |A_{\ell'}|^2 |\langle \ell' 010|\ell 0\rangle|^2 |Y_{\ell 0}(\theta)|^2 \qquad \text{(A1)}$$

where $\langle \ell' 010|\ell 0\rangle$ is a Clebsch–Gordan coefficient. Due to the properties of these coefficients we can write

$$P_{i\to f}(\theta) = \sum_{\ell} |B_\ell|^2 \frac{|A_{\ell-1}|^2 \ell(3+2\ell) + |A_\ell + 1|^2 (2\ell^2 + \ell - 1)}{4\ell(1+\ell) - 3}$$

$$|Y_{\ell 0}(\theta)|^2 \equiv \sum_{j=0}^{\infty} D_j P_{2j}(\cos\theta) \qquad \text{(A2)}$$

where $P_j(x)$ are the Legendre polynomials of order j. If the involved states are limited to $\ell \leq 1$

$$\varphi_i(\theta) = Y_{00} + A_1 Y_{10}(\theta)$$

$$\varphi_f(\theta) = Y_{00} + B_1 Y_{10}(\theta),$$

we obtain for the transition probability

$$P_{i\to f}(\theta) = \frac{|A_1|^2}{12\pi} + \frac{3|B_1|^2}{4\pi}\cos^2(\theta) \propto 1 + \frac{2}{1 + |A_1|^2/(3|B_1|^2)} P_2(\cos\theta) \equiv 1 + \beta P_2(\cos\theta) \qquad \text{(A3)}$$

It can be seen that the anisotropy can only take positive values. When $|B_1|^2 > |A_1|^2$, the anisotropy is constrained to $1.5 < \beta < 2$, and if the initial state is spherical ($A_1 = 0$) one finds the limiting value $\beta = 2$.

When non-axially symmetric deformations are included ($m \neq 0$) the transition probability for $\ell \leq 1$ reads

$$P_{i\to f}(\theta) = \sum_{\ell\ell' \leq 1, mm'} |B_{\ell m}|^2 |A_{\ell' m'}|^2 |\langle \ell' m' 10|\ell m\rangle|^2 |Y_{\ell 0}(\theta)|^2 \propto 1 + \beta_0 K P_2(\cos\theta) \qquad \text{(A4)}$$

with $\beta_0 = 2/(1 + |A_{10}|^2/(3|B_{10}|^2))$ [the same structure as in eqn (A3)] and

$$K = \frac{(|A_{10}|^2 + 3|B_{10}|^2)(4|B_{10}|^2 - |A_{11}|^2|B_{11}|^2 - |A_{1-1}|^2|B_{1-1}|^2)}{2|B_{10}|^2[2(|A_{10}|^2 + 3|B_{10}|^2) + 3(|A_{11}|^2|B_{11}|^2 + |A_{1-1}|^2|B_{1-1}|^2)]}. \qquad \text{(A5)}$$

Some algebra shows that $K < 1$, since $(|A_{10}|^2 + 9|B_{10}|^2)(|A_{11}|^2|B_{11}|^2 + |A_{1-1}|^2|B_{1-1}|^2) > 0$. Consequently, these deformations will always decrease the value of the anisotropy parameter.

Appendix B

We show in this appendix how we have represented the delta functions involved in eqn (16) to compute the GR. Using the rectangular function $\mathrm{rect}(x) \equiv \vartheta(x + 1/2) - \vartheta(x - 1/2)$, where $\vartheta(x)$ is the Step function, we write

$$w_{i\to f} \propto [1 + \beta P_2(\cos\theta)] \frac{1}{M} \sum_{i=1}^{M} \mathrm{rect}\left[\frac{\hbar\mathbf{k} - m_{\mathrm{Na}}\dot{\mathbf{R}}_i(t_\infty)}{\Delta k}\right] \frac{1}{\Delta k} \mathrm{rect}\left[\frac{\hbar\omega - [V_{\mathrm{Na}}^{4s}(0, \mathbf{R}_i(0)) - \hbar\omega_{\mathrm{gs}}]}{\Delta\omega}\right] \frac{1}{\Delta\omega}, \qquad \text{(B1)}$$

where we have used for the number of test particles $M = 200\,000$ and the intervals take small values as $\Delta k/m_{\mathrm{Na}} \approx 5$ m s^{-1} and $\Delta\omega \approx 3$ K. The velocity distributions are simulated by choosing a value of the excitation energy ω and evaluating eqn (B1), while the final kinetic energy *vs.* excitation energy distribution is obtained after the change of variable $E_k = \hbar^2 k^2/2m_{\mathrm{Na}}$ as

$$I(\omega, E_k) = \sqrt{\frac{m_{\mathrm{Na}}}{2E_k\hbar^2}} I\left(\omega, k = \sqrt{\frac{2m_{\mathrm{Na}}E_k}{\hbar^2}}\right) = \frac{1}{M}\sum_{i=1}^{M} \mathrm{rect}\left[\frac{E_k - m_{\mathrm{Na}}\dot{\mathbf{R}}_i^2(t_\infty)/2}{\Delta E_k}\right] \frac{1}{\Delta E_k} \mathrm{rect}\left[\frac{\hbar\omega - [V_{\mathrm{Na}}^{4s}(0, \mathbf{R}_i(0)) - \hbar\omega_{\mathrm{gs}}]}{\Delta\omega}\right] \frac{1}{\Delta\omega}. \qquad \text{(B2)}$$

The excitation spectrum is computed as

$$I(\omega) = \frac{1}{M}\sum_{i=1}^{M} \mathrm{rect}\left[\frac{\hbar\omega - [V_{\mathrm{Na}}^{4s}(0, \mathbf{R}_i(0)) - \hbar\omega_{\mathrm{gs}}]}{\Delta\omega}\right] \frac{1}{\Delta\omega}. \qquad \text{(B3)}$$

If density fluctuations are included using the stochastic method described in detail in ref. 14 and 46, the total distribution is generated by the contribution of N_c configurations generated by sorting N random positions in the j-th configuration $\{\mathbf{r}_n^j\}_{n=1}^N$ for the hard spheres that represent the N helium atoms, using the helium density divided by N as probability density distribution together with a hard-sphere repulsion between He atoms. The diameter of the sphere is of the order of the length h used to screen the Lennard-Jones potential and

to compute the coarse-grained density.[31] This diameter is defined as[14,46]

$$d_n^j = h\left(\frac{\rho_0}{\bar{\rho}(\mathbf{r}_n^j)}\right)^{1/3}, \tag{B4}$$

where ρ_0 is the liquid saturation density value, and $\bar{\rho}$ is the coarse-grained density obtained by averaging the atomic density within a sphere of radius h.[31] The distributions are then obtained as

$$w_{i\to f} \propto \frac{1}{N_c}\sum_{j=1}^{N_c}\sum_{n=1}^{N}[1+\beta P_2(\cos\theta)]\frac{1}{M} \sum_{i=1}^{M}\mathrm{rect}\left[\frac{\hbar\mathbf{k}-m_{Na}\dot{\mathbf{R}}_i(t_\infty)}{\Delta k}\right] \frac{1}{\Delta k}\mathrm{rect}\left[\frac{\hbar\omega-[V_X^{4s}(|\mathbf{r}_n^j-\mathbf{R}_i(0)|)-\hbar\omega_{gs}]}{\Delta\omega}\right]\frac{1}{\Delta\omega}, \tag{B5}$$

$$I(\omega,E_k) = \frac{1}{N_c}\sum_{j=1}^{N_c}\sum_{n=1}^{N}\frac{1}{M}\sum_{i=1}^{M}\mathrm{rect}\left[\frac{E_k-m_{Na}\dot{\mathbf{R}}_i^2(t_\infty)/2}{\Delta E_k}\right] \frac{1}{\Delta E_k}\mathrm{rect}\left[\frac{\hbar\omega-[V_X^{4s}(|\mathbf{r}_n^j-\mathbf{R}_i(0)|)-\hbar\omega_{gs}]}{\Delta\omega}\right]\frac{1}{\Delta\omega}, \tag{B6}$$

and

$$I(\omega) = \frac{1}{N_c}\sum_{j=1}^{N_c}\sum_{n=1}^{N}\frac{1}{M}\sum_{i=1}^{M}\mathrm{rect}\left[\frac{\hbar\omega-[V_X^{4s}(|\mathbf{r}_n^j-\mathbf{R}_i(0)|)-\hbar\omega_{gs}]}{\Delta\omega}\right]\frac{1}{\Delta\omega}. \tag{B7}$$

Note that with a number of configurations $N_c = 10\,000$, the histograms are computed using a total of $N_c \times M = 2 \times 10^9$ contributions, large enough to reduce the statistical noise.

Acknowledgements

We would like to thank David Mateo for useful discussions. This work has been performed under Grants No. FIS2008-00421/FIS from DGI, Spain (FEDER), 2009SGR1289 from Generalitat de Catalunya, and 200020-119789 from the Swiss National Science Foundation. AH has been supported by the ME (Spain) FPI program, Grant No. BES-2009-027139.

References

1 Y. Kwon, P. Huang, M. V. Patel, D. Blume and K. B. Whaley, *J. Chem. Phys.*, 2000, **113**, 6469.
2 F. Stienkemeier and A. F. Vilesov, *J. Chem. Phys.*, 2001, **115**, 10119.
3 J. P. Toennies and A. F. Vilesov, *Angew. Chem., Int. Ed.*, 2004, **43**, 2622.
4 M. Barranco, R. Guardiola, S. Hernández, R. Mayol, J. Navarro and M. Pi, *J. Low Temp. Phys.*, 2006, **142**, 1.
5 F. Stienkemeier and K. K. Lehmann, *J. Phys. B: At., Mol. Opt. Phys.*, 2006, **39**, R127.
6 M. Y. Choi, G. E. Douberly, T. M. Falconer, W. K. Lewis, C. M. Lindsay, J. M. Merrit, P. L. Stiles and R. E. Miller, *Int. Rev. Phys. Chem.*, 2006, **25**, 15.
7 J. Tiggesbäumker and F. Stienkemeier, *Phys. Chem. Chem. Phys.*, 2007, **9**, 4748.
8 K. Szalewicz, *Int. Rev. Phys. Chem.*, 2008, **27**, 273.
9 O. Birer, P. Moreschini and K. K. Lehmann, *Phys. Chem. Chem. Phys.*, 2008, **10**, 1648.
10 E. Loginov, D. Rossi and M. Drabbels, *Phys. Rev. Lett.*, 2005, **95**, 163401.
11 F. Stienkemeier, J. Higgins, C. Callegari, S. I. Kanorsky, W. E. Ernst and G. Scoles, *Z. Phys. D: At., Mol. Clusters*, 1996, **38**, 253.
12 J. Reho, C. Callegari, J. Higgins, W. E. Ernst, K. K. Lehmann and G. Scoles, *Faraday Discuss.*, 1997, **108**, 161.
13 O. Bünermann, G. Droppelmann, A. Hernando, R. Mayol and F. Stienkemeier, *J. Phys. Chem. A*, 2007, **111**, 12684.
14 A. Hernando, M. Barranco, R. Mayol, M. Pi, F. Ancilotto, O. Bünermann and F. Stienkemeier, *J. Low Temp. Phys.*, 2010, **158**, 105.
15 A. Nakayama and K. Yamashita, *J. Chem. Phys.*, 2001, **114**, 780.
16 E. Loginov and M. Drabbels, *Phys. Rev. Lett.*, 2011, **106**, 083401.
17 E. Loginov, C. Callegari, F. Ancilotto and M. Drabbels, *J. Phys. Chem. A*, 2011, **115**, 6779.
18 A. Pifrader, O. Allard, G. Auböck, C. Callegari, W. E. Ernst, R. Huber and F. Ancilotto, *J. Chem. Phys.*, 2010, **133**, 164502.
19 J. Reho, J. Higgins, K. K. Lehmann and G. Scoles, *J. Chem. Phys.*, 2000, **113**, 9694.
20 C. P. Schulz, P. Claas and F. Stienkemeier, *Phys. Rev. Lett.*, 2001, **87**, 153401.
21 D. Bohm, *Phys. Rev.*, 1952, **85**, 166; D. Bohm, *Phys. Rev.*, 1952, **85**, 180.
22 R. E. Wyatt, *J. Chem. Phys.*, 1999, **111**, 4406.
23 M. Guilleumas, M. Pi, M. Barranco and E. Suraud, *Z. Phys. D: At., Mol. Clusters*, 1995, **34**, 35.
24 R. E. Wyatt, *Quantum Dynamics with Trajectories*, Springer, New York, 2005.
25 R. E. Wyatt Festschrift, *J. Phys. Chem. A*, 2007, **111**, 10171–10433.
26 P. K. Chattaraj, *Quantum Trajectories*, CRC Press, Boca Raton, 2011.
27 A. Braun and M. Drabbels, *J. Chem. Phys.*, 2007, **127**, 114303.
28 E. Loginov and M. Drabbels, *J. Phys. Chem. A*, 2007, **111**, 7504.
29 M. Lewerenz, B. Schilling and J. P. Toennies, *Chem. Phys. Lett.*, 1993, **206**, 381.
30 M. Weissbluth, *Atoms and molecules*, Academic Press, New York, 1980; F. O. Ellison, *J. Am. Chem. Soc.*, 1963, **85**, 3540.
31 F. Dalfovo, A. Lastri, L. Pricaupenko, S. Stringari and J. Treiner, *Phys. Rev. B: Condens. Matter Mater. Phys.*, 1995, **52**, 1193.
32 R. N. Zare, *Mol. Photochem.*, 1972, **4**, 1.
33 R. N. Zare, *Angular momentum*, John Wiley & Sons, New York, 1988.
34 S. H. Patil, *J. Chem. Phys.*, 1991, **94**, 8089.
35 J. Pascale, *Phys. Rev. A: At., Mol., Opt. Phys.*, 1983, **28**, 632.
36 A. Hernando, M. Barranco, R. Mayol, M. Pi and M. Krosnicki, *Phys. Rev. B: Condens. Matter Mater. Phys.*, 2008, **77**, 024513.
37 A. Hernando, M. Barranco, R. Mayol, M. Pi and F. Ancilotto, *Phys. Rev. B: Condens. Matter Mater. Phys.*, 2008, **78**, 184515.
38 M. Lax, *J. Chem. Phys.*, 1952, **20**, 1752.
39 D. Zwillinger, *Handbook of Differential Equations*, Academic Press, Boston, 3rd edn, 1997.
40 A. Wada, T. Takayanagi and M. Shiga, *J. Chem. Phys.*, 2003, **119**, 5478.
41 T. Takayanagi and M. Shiga, *Chem. Phys. Lett.*, 2003, **372**, 90.
42 T. Takayanagi and M. Shiga, *Phys. Chem. Chem. Phys.*, 2004, **6**, 3241.
43 D. Bonhommeau, P. T. Lake Jr., C. Le Quiniou, M. Lewerenz and N. Halberstadt, *J. Chem. Phys.*, 2007, **126**, 051104.
44 D. Bonhommeau, M. Lewerenz and N. Halberstadt, *J. Chem. Phys.*, 2008, **128**, 054302.
45 A. Hernando, R. Mayol, M. Pi, M. Barranco, I. S. K. Kerkines and A. Mavridis, *Int. J. Quantum Chem.*, 2011, **111**, 400.
46 D. Mateo, A. Hernando, M. Barranco, R. Mayol and M. Pi, *Phys. Rev. B: Condens. Matter Mater. Phys.*, 2011, **83**, 174505.
47 O. Bünermann, M. Dvorak, F. Stienkemeier, A. Hernando, R. Mayol, M. Pi, M. Barranco and F. Ancilotto, *Phys. Rev. B: Condens. Matter Mater. Phys.*, 2009, **79**, 214511.
48 Y. Ralchenko, A. E. Kramida and J. Reader and NIST ASD Team, *NIST Atomic Spectra Database (version 3.1.5)*, National Institute of Standards and Technology, Gaithersburg, MD, 2008.

49 M. Aymar, E. Luckoenig and F. C. Farnoux, *J. Phys. B: At., Mol. Opt. Phys.*, 1976, **9**, 1279.
50 M. Aymar, *J. Phys. B: At., Mol. Opt. Phys.*, 1978, **11**, 1413.
51 C. Callegari and F. Ancilotto, *J. Phys. Chem. A*, 2011, **115**, 6789.
52 C. Callegari, private communication.
53 G. E. Busch and K. R. Wilson, *J. Chem. Phys.*, 1972, **56**, 3638.
54 Above an excitation energy of 26 400 cm^{-1} the data points clearly deviate from the linear dependence observed at lower energies and therefore have not been included in the fit.
55 We recall that the sound velocity in superfluid ^{4}He at zero pressure and temperature is 238 m s^{-1}, see *e.g.* J. Wilks, *The properties of liquid and solid helium*, Clarendon Press, Oxford, 1967.
56 J. Eloranta and V. A. Apkarian, *J. Chem. Phys.*, 2002, **117**, 10139.
57 D. Mateo, D. Jin, M. Barranco and M. Pi, *J. Chem. Phys.*, 2011, **134**, 044507.
58 C. G. Morgan, M. Drabbels and A. M. Wodtke, *Adv. Photochem.*, 1997, **23**, 279.
59 G. E. Busch and K. R. Wilson, *J. Chem. Phys.*, 1972, **56**, 3626.
60 A. Braun and M. Drabbels, *Phys. Rev. Lett.*, 2004, **93**, 253401.
61 A. Braun and M. Drabbels, *J. Chem. Phys.*, 2007, **127**, 114304.
62 J. L. Persson, Q. Hui, Z. J. Jakubek, M. Nakamura and M. Takami, *Phys. Rev. Lett.*, 1996, **76**, 1501.
63 G. Droppelmann, O. Bünermann, C. P. Schulz and F. Stienkemeier, *Phys. Rev. Lett*, 2004, **93**, 023402.
64 K. Enomoto, K. Hirano, M. Kumakura, Y. Takahashi and Y. Yabuzaki, *Phys. Rev. A: At., Mol., Opt. Phys.*, 2004, **69**, 012501.

